Radiative forcing under mixed aerosol conditions

O. E. García,[1,2] F. J. Expósito,[1] J. P. Díaz,[1] and A. M. Díaz[1]

Received 11 December 2009; revised 2 September 2010; accepted 24 September 2010; published 6 January 2011.

[1] The mixture of mineral dust with biomass burning or urban-industrial aerosols presents significant differences in optical properties when compared to those of the individual constituents, leading to different impacts on solar radiation levels. This effect is assessed by estimating the direct radiative forcing (ΔF) of these aerosols from solar flux models using the radiative parameters derived from the Aerosol Robotic Network (AERONET). These data reveal that, in oceanic and vegetative covers (surface albedo (SA) < 0.30), the aerosol effect at the top of atmosphere (TOA) is always cooling the Earth-atmosphere system, regardless of the aerosol type. The obtained average values of ΔF range between -27 ± 15 Wm^{-2} (aerosol optical depth (AOD) at 0.55 μm, 0.3 ± 0.3) for mineral dust mixed with urban-industrial aerosols, registered in the East Asia region, and -34 ± 18 Wm^{-2} (AOD = 0.8 ± 0.4) for the mixture of the mineral dust and biomass burning particles, observed in the Central Africa region. In the intermediate SA range (0.30–0.50) the TOA radiative effect depends on the aerosol absorption properties. Thus, aerosols with single scattering albedo at 0.55 μm lower than ~0.88 lead to a warming of the system, with ΔF of 10 ± 11 Wm^{-2} for the mixture of mineral dust and biomass burning. Cases with SA > 0.30 are not present in East Asia region. At the bottom of atmosphere (BOA) the maximum ΔF values are associated with the highest AOD levels obtained for the mixture of mineral dust and biomass burning aerosols (-130 ± 44 Wm^{-2} with AOD = 0.8 ± 0.4 for SA < 0.30).

Citation: García, O. E., F. J. Expósito, J. P. Díaz, and A. M. Díaz (2011), Radiative forcing under mixed aerosol conditions, *J. Geophys. Res.*, *116*, D01201, doi:10.1029/2009JD013625.

1. Introduction

[2] Even though the impact of atmospheric aerosols on climate (and climatic change) is undeniable, quantification of their radiative forcing (direct, semidirect, and indirect effects) is still uncertain [*IPCC*, 2007]. The radiative effects of these atmospheric constituents depend largely on both their size distributions and their chemical composition. On a global scale, the direct radiative forcing of sulphates is estimated to be -0.4 ± 0.2 Wm^{-2}, with organic carbon -0.05 ± 0.05 Wm^{-2} and soot $+0.20 \pm 0.15$ Wm^{-2}, while aerosol radiative forcing from natural origins such as biomass burning and mineral dust are $+0.03 \pm 0.12$ Wm^{-2} and -0.1 ± 0.2 Wm^{-2}, respectively [*IPCC*, 2007]. These values clearly indicate significant uncertainties and confirm the need to study their properties and to quantify their effects on radiative balance.

[3] Among the different types of aerosols in the atmosphere, desert mineral dust plays a fundamental role in the energy balance of the Earth-atmosphere system due to its high emission rate, 1000–2150 Tg·yr^{-1} [e.g., *Satheesh and Moorthy*, 2005; *IPCC*, 2007], and the broad area over which it extends, causing the "global dust belt" (~5°–40°N) [*Prospero et al.*, 2002, and references therein]. In this regard, recent studies have focused on determining the radiative forcing of pure mineral dust [e.g., *García*, 2009, and references therein], but few have evaluated the effect when it is mixed with other types such as biomass burning or urban-industrial aerosols. These cases are especially important because the radiative properties of this atmospheric constituent change. For example, a mixture with particles from biomass burning increases the absorption of the mineral dust, resulting in greater impact of this component on the Earth-atmosphere system [*Arimoto et al.*, 2006]. In this regard, for example, *Derimian et al.* [2008] found that in some cases the mixture of mineral dust and biomass burning aerosols can reduce the solar radiation reaching the surface by almost double that of dust alone.

[4] *Gu et al.* [2006] in their study of the climatic effects of different aerosols types in China used simulated data in the University of California, Los Angeles Atmospheric General Circulation Model (UCLA AGCM) general circulation model. They studied five different aerosols situations, in which their DUST model involved 90% large mineral dust particles (8.0 μm) and 10% soot, while their SOOT model used 100% soot. They found radiative forcing values at top of atmosphere (TOA) of 30.97 Wm^{-2} and 21.71 Wm^{-2} for SOOT and DUST models, respectively. Moreover, *Chung and Seinfeld* [2005] and *Hansen and Nazarenko* [2004]

[1]Grupo de Observación de la Tierra y la Atmósfera, Universidad de La Laguna, La Laguna, Tenerife, Spain.
[2]Now at Centro de Investigación Atmosférico de Izaña, Agencia Estatal de Meteorología, Santa Cruz de Tenerife, Tenerife, Spain.

0148-0227/11/2009JD013625

studied the climate response of direct radiative forcing of anthropogenic black carbon (BC), finding that the radiative forcing of this compound is different depending on whether BC is externally or internally mixed. *Martins et al.* [1998] show how the radiative properties of BC are changed in external or internal mixture models.

[5] This paper analyzes and assesses the impact of the mixtures of mineral dust with biomass burning and urban-industrial aerosols, using particles sizes from 0.05 to 15 μm, on the Earth's radiation balance.

2. Methodology and Data

2.1. AERONET Data

[6] The Aerosol Robotic Network (AERONET) is one of the most useful global networks for the monitoring of atmospheric aerosols. It collects near real-time observations of spectral and columnar integrated aerosol optical properties. These data are collected by automatic Sun and sky scanning spectral radiometers manufactured by CIMEL Electronique and they are distributed to worldwide locations [*Holben et al.*, 2001]. The CIMEL radiometers can be accessed by different models and direct Sun measurements are available on all or some of the 0.34, 0.38, 0.44, 0.50, 0.67, 0.87, 0.94, 1.02, and 1.64 μm (nominal wavelengths) channels, retrieving aerosol optical depth (AOD) at all these wavelengths, except at 0.94 μm which is used to estimate total precipitable water content. In addition to the direct solar radiance measurements, which are made with a field of view of 1.2°, these instruments measure the sky radiance in four spectral bands (0.44, 0.67, 0.87, and 1.02 μm) along both the solar principal plane and the solar almucantar.

[7] Solar aureole and sky radiance together with Sun measurements are used to retrieve aerosol volume size distributions (from 0.05 to 15 μm), spectral complex refractive index ($m(\lambda) - ik(\lambda)$) and single scattering albedo ($\omega(\lambda)$) at low solar elevations (solar zenith angle between 50° and 80°), following a flexible inversion algorithm developed by *Dubovik and King* [2000] (version 1.0, inversion products). This algorithm uses models of homogeneous spheres and randomly oriented spheroids [*Dubovik et al.*, 2002]. Recently a new version of this inversion algorithm has been developed (Version 2.0), where the most significant modification is the use of a spheroid mixture as a generalized aerosol model (representing spherical, nonspherical, and mixed aerosols) [*Dubovik et al.*, 2006] and replacing the spherical and spheroid models used separately up to now. In this vein, Version 2.0 provides parameterization of the degree of nonsphericity (sphericity parameter), as well as the same set of retrieved aerosol parameters given in Version 1.0. Another important improvement in Version 2.0 is the assumption of a dynamic spectral and spatial satellite and model estimation of the surface albedo, including the bidirectional reflectance distribution function (BRDF), in place of assumed surface reflectivity [*Dubovik et al.*, 2002]. The BRDF Cox-Munk model over water [*Cox and Munk*, 1954] was used, which takes into account the wind effect over water using wind speed data from the National Centers for Environmental Prediction/National Center for Atmospheric Research (NCEP/NCAR) database (NOAA Operational Model Archive Distribution System server at NCEP). For land surface covers, the Lie-Ross model was adopted [*Lucht and Roujean*, 2000], where the BRDF parameters are taken from the Moderate Resolution Imaging Spectroradiometer (MODIS) Ecotype generic BRDF models for vegetation, snow, and ice [*Nolin et al.*, 1998; *Hall et al.*, 2002; *Moody et al.*, 2005]. Finally, in Version 2.0 a set of radiative quantities are given at any AERONET station, including spectral and broadband fluxes, aerosol radiative forcing, and aerosol radiative forcing efficiency, both at the TOA and bottom of atmosphere (BOA), using the radiative transfer model explained in detail in section 2.2.

[8] The AERONET data used in this study are from Version 2.0, Level 2.0, are cloud screened and quality ensured (AERONET Version 2.0 quality assurance criteria (V2-AQC), and are available at http://aeronet.gsfc.nasa.gov/).

2.2. Radiative Transfer Model

[9] Direct aerosol radiative forcing, ΔF, is defined as the difference between the global solar irradiance with and without aerosol presence, F^A and F^C respectively. In the literature, this magnitude is normally referred to the BOA and the TOA, yielding the expressions

$$\begin{aligned} \Delta F_{BOA} &= F_{BOA}^{\downarrow A} - F_{BOA}^{\downarrow c} \\ \Delta F_{TOA} &= F_{TOA}^{\uparrow c} - F_{TOA}^{\uparrow A} \end{aligned}, \tag{1}$$

where the arrows indicate the direction of the global fluxes, $\downarrow$ indicating downward flux and $\uparrow$ indicating upward flux. This sign criterion implies that negative values of ΔF at the BOA and the TOA are associated with an aerosol cooling effect, while a warming effect is due to positive values of ΔF at the BOA and the TOA.

[10] The solar broadband fluxes were calculated for solar zenith angles between 50° and 80°, by spectral integration in the range from 0.2 to 4.0 μm, using more than 200 size subintervals. In each of these subintervals the phase function was calculated using the retrieved size distribution in the exact same manner as in the AERONET retrieval scheme. The values of $m(\lambda)$ and $k(\lambda)$ were interpolated/extrapolated from the values $m(\lambda)$ and $k(\lambda)$ retrieved at AERONET wavelengths. Likewise, spectral dependence of surface reflectance is interpolated/extrapolated from surface albedo values assumed in the retrieval on the wavelengths of Sun/sky-radiometer. Similar to the AERONET retrieval approach, the flux calculations accounted for the absorption and multiple scattering effects using the Discrete Ordinates (DISORT) approach [*Stamnes et al.*, 1988; *Nakajima and Tanaka*, 1988].

[11] The integration of atmospheric gaseous absorption and molecular scattering effects were conducted using developments employed in the Global Atmospheric Model (GAME) code [*Dubuisson et al.*, 1996; *Roger et al.*, 2006]. In the GAME code, gaseous absorption (mainly H_2O, CO_2, and O_3) is calculated from the correlated k distribution [*Lacis and Oinas*, 1991]. The correlated k distribution allows for the interactions between gaseous absorption and multiple scattering to be accounted for with manageable computational time. Coefficients of the correlated k distribution were estimated from reference calculations using a line-by-line code [*Dubuisson et al.*, 2004]. Regarding the gaseous content in the atmospheric column, the instantaneous water vapor content retrieved by AERONET, using the absorption

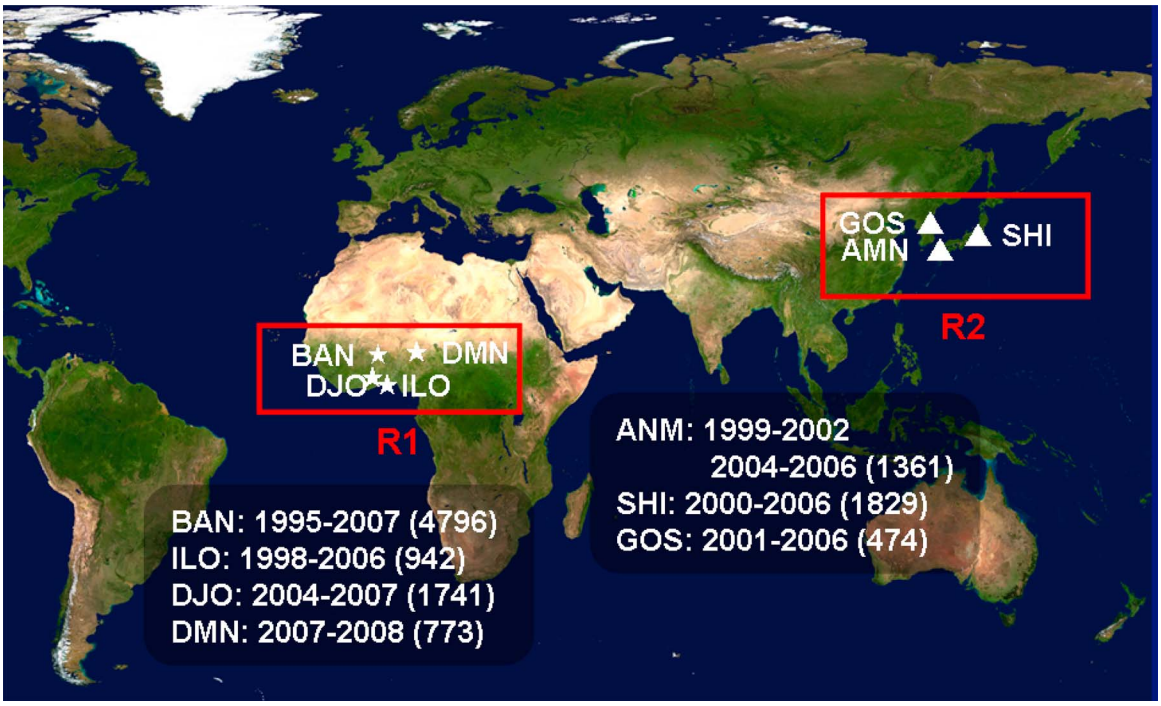

Figure 1. Geographical distribution of the AERONET stations used. BAN, Banizoumbou; ILO, Ilorin; DJO, Djougou; and DMN, DMN Maine Soroa stations in region 1 (R1). GOS, Gosan; ANM, Anmyon; and SHI, Shiranama stations in region 2 (R2). Also, the period and number of data for each station are shown.

differential method at the 0.94 μm channel [*Smirnov et al.*, 2004] was employed, whereas the total ozone content was taken from monthly climatology values (1978–2004) based on the NASA Total Ozone Mapping Spectrometer (TOMS) measurements (available at http://jwocky.gsfc.nasa.gov/). The GAME model accounts for spectral gaseous absorption: Ozone in the ultraviolet-visible spectral ranges (0.2–0.35 μm and 0.5–0.7 μm) and water vapor in the shortwave infrared spectrum (0.8–3 μm). The atmospheric gaseous profile (US standard 1976 atmosphere model) was scaled to match with the gaseous concentrations in column. The GAME code has a fixed spectral resolution of 100 cm^{-1} from 2500 to 17,700 cm^{-1} (4–0.6 μm) and 400 cm^{-1} from 17,700 cm^{-1} to 50,000 cm^{-1} (0.6–0.2 μm).

[12] This radiative transfer model was previously validated using ground-based solar measurements by the Baseline Surface Radiation Network (BSRN) and Solar Radiation Network (SolRad-Net) global networks, and at the Mauna Loa Observatory (MLO) under different aerosol regimens [*García et al.*, 2008a]. As a result, in global terms, a small overestimation of 9 ± 12 Wm^{-2} for measured radiation was found. For the aerosols considered in the current work these differences are 16 ± 10 Wm^{-2} for mineral dust, 14 ± 10 Wm^{-2} for urban-industrial, and 6 ± 13 Wm^{-2} for biomass burning aerosols. Ground-based measurements only allow directly solar fluxes and ΔF values at the BOA to be validated. However errors of the same order of magnitude are expected for these parameters at the TOA, since the same methodology (e.g., aerosol and gaseous characterization, radiative model) is applied to calculate the radiative magnitudes at both the BOA and the TOA.

[13] The homogeneous aerosol vertical structure in the model assumptions in the AERONET retrievals can also be considered as sources of uncertainty; however, the effect of these errors is minor in most cases [*Dubovik et al.*, 2000]. The flux calculations are performed for multilayered atmosphere with the US standard atmosphere model for gaseous distributions and single fixed aerosol vertical distribution (exponential with aerosol height of 1 km). The assumption changes in this study may not reflect actual atmospheric conditions and are also potential source of errors; however, our tests did not show any significant sensitivity of flux estimates for these assumptions [*García et al.*, 2008a]. Differences of less than 1 Wm^{-2} due to different vertical profiles were observed on the downward solar flux at the BOA. The sensitivity tests were conducted for AOD(0.55 μm) of 0.1, 0.5, and 1.0, and separately for the two aerosol types: 1. Size distribution with dominant coarse mode and increased absorption at 440 nm (mineral dust conditions); and 2. bimodal size distribution absorbing aerosols (anthropogenic situation). These differences are negligible (~0.2–3%) compared to instantaneous aerosol radiative forcing. Thus this strategy, concerning the use of external or internal mixtures, is very good at obtaining the radiative forcing values independent of the actual mixture state.

3. Site Descriptions

[14] In this work, AERONET stations were selected to assess mixtures of mineral dust with biomass burning or urban-industrial aerosols. The data from the stations were characterized by long-term time series and grouped into two regions. Figure 1 shows the locations of the stations used.

The selected observatories in region 1, Banizoumbou (BAN), Ilorin (ILO), Djougou (DJO), and DMN Maine Soroa (DMN), are very close to the Sahara-Sahel desert area (20°–30°N, 16°W–35°E) and immersed in the Central African savanna. They are frequently affected by high emission rates of biomass burning and mineral dust, although the presence of the latter is continuous throughout the year [*Prospero et al.*, 2002, and references therein]. The main source areas of the crustal material are the desert areas of Niger, southern Algeria and Libya, and Bodele Depression in the Lake Chad Basin [*Holben et al.*, 2001; *Prospero et al.*, 2002]. The second group (region 2) includes stations from East Asia, Anmyon (ANM), Gosan (GOS), and Shirahama (SHI), where urban-industrial emissions are dominant throughout the year along with major episodes of mineral dust from the Taklamakan desert in the Tarim Basin Pendi (36°–40°N, 75°–90°E) and the Gobi desert (42°–45°N, 100°–110°E). Unlike the mineral dust production processes in the Taklamakan desert, which are almost constant throughout the year, the Gobi desert shows a marked seasonal variation (maximum in spring and early summer), due to Gobi dust storms usually occur in response to strong winter storms that emerge from Siberia [*Prospero et al.*, 2002, and references therein].

3.1. Region 1: Mineral Dust and Biomass Burning

[15] In region 1 the mixture of mineral dust and aerosols generated from biomass burning occurs mainly during the winter, December–February (DJF), which is the season of maximum activity of biomass burning in Central Africa. In this period maximum values of AOD are obtained (~1.2 at 0.55 μm) diminishing during the summer, from June–August (JJA), with values of AOD(0.55 μm) between 0.2 and 0.6, when aerosol emissions are dominated by crustal material from desert areas (Figure 2a). The summer and early autumn is the rainy season, favored by the northernmost position of the InterTropical Convergence Zone (ITCZ). In this period phenomena of wet deposition of mineral dust are common and, therefore, minimum annual values of AOD are observed (Figure 2a). For instance, the interannual average of AOD(0.55 μm) at Ilorin station is 0.8 ± 0.5, with mean AOD values greater than 0.6 throughout the winter and early spring (March–May, MAM).

[16] In order to distinguish the predominant aerosol, monthly average values of three parameters at 0.55 μm were analyzed. These parameters were: the fine aerosol fraction, η, which is the fraction of the total optical depth attributed to the fine mode particle size distribution (Figure 2b), the single scattering albedo, ω (Figure 2c), and the asymmetry factor, g (Figure 2d). The effective radius was also taken into account (Figure 2e). The combination of that information allows us to discriminate between aerosols with similar sizes but with different radiative footprints, such as mineral dust and biomass burning particles [*Kaufman et al.*, 2005]. In this region the winter months are dominated by high AOD values. The observed data of η (~0.3–0.6) are lower than the values of pure biomass burning, which are between 0.7 and 1.0 [*Kaufman et al.*, 2005], and indicate combined contributions of mineral dust and biomass burning [*Holben et al.*, 2001]. Lower single scattering albedo and effective radius are also recorded. Consequently the aerosol mixture in winter has a greater absorption capacity than the pure mineral, since biomass burning particles (elemental carbon) enhance the absorption of solar radiation (higher imaginary part of refractive index) [*Arimoto et al.*, 2006; *Lyamani et al.*, 2006; *Derimian et al.*, 2008; *García et al.*, 2008b]. For example, during the winter the interannual average of single scattering albedo derived by AERONET, ω(0.44/0.67/0.87/1.02 μm) = 0.84/0.88/0.90/0.91 ± (0.04–0.05) and ω = 0.83/0.86/0.87/0.88 ± (0.05–0.07) for Ilorin and Djougou, respectively, are lower than those observed at these stations during the rest of the year of ω = 0.90/0.94/0.95/0.96 ± 0.04 in Ilorin and ω = 0.89/0.93/0.95/0.96 ± 0.04 at Djougou, revealing most absorbing aerosols during winter (Figure 2c). Similar behavior was observed for other radiative properties, such as for the imaginary part of the refractive index (data not shown).

[17] Moreover, as is shown in Figures 2a and 2b, during the spring the values of the fine fraction decrease, which is associated with a reduction of the biomass burning contribution. During this season AOD levels decrease but remain between 0.5 and 0.9, and minimum values of η (0.3–0.4) were observed. The single scattering albedo remains constant between 0.90 and 0.95, and the effective radius shows the highest values for the four stations. All of these characteristics correspond to a situation where the predominant aerosol is the mineral dust.

[18] In order to compare the radiative effect of mineral dust mixed with biomass burning and pure mineral dust, the winter (DJF) and spring (MAM) seasons, respectively, were selected. In both cases, mineral dust is the dominant aerosol as is observed in the regional and interannual average of the radiative properties, as well as the size and shape parameters during these seasons, as is shown in Table 1. The average values of AOD, η, g and the effective radius (r_{eff}) are evaluated with the total dataset (Figure 2). However, the single scattering albedo, complex refractive index, and sphericity parameter (Esf.) are calculated with only those data that satisfy the V2-QAC criteria used in AERONET Version 2 (AOD(0.44 μm) $\geq$ 0.4 for ω, m, and k, and AOD (0.44 μm) $\geq$ 0.2 for the sphericity parameter). Therefore, considering these aerosol properties, winter and spring are predominantly characterized by large and nonspherical particles (high effective radius, $r_{\text{eff}} > 0.6$ μm, and low sphericity parameter, <7%). In addition, the spectral dependence of the single scattering albedo reveals a greater absorption at shorter and near ultraviolet wavelengths. This behavior is typical of mineral dust, and contrary to biomass burning particles, where the absorption increases in the near infrared [e.g., *D'Almeida et al.*, 1991; *Dubovik et al.*, 2002]. Note that the ω values are lower in winter than spring, showing the presence of aerosols with greater absorption capacities during this period, as mentioned previously. Thus, it is possible to confirm that the crustal material is the dominant aerosol in the region.

3.2. Region 2: Urban-Industrial and Mineral Dust

[19] Although aerosols in region 2 are predominantly urban and industrial, three different periods can be indentified (Figures 3a–3e) based on the interannual average values of aerosol optical depth, the fine aerosol fraction, single scattering albedo, asymmetry factor, and effective radius. The season of mineral dust outbreaks is quite clear in all locations (from March–May) where there is an increase of AOD

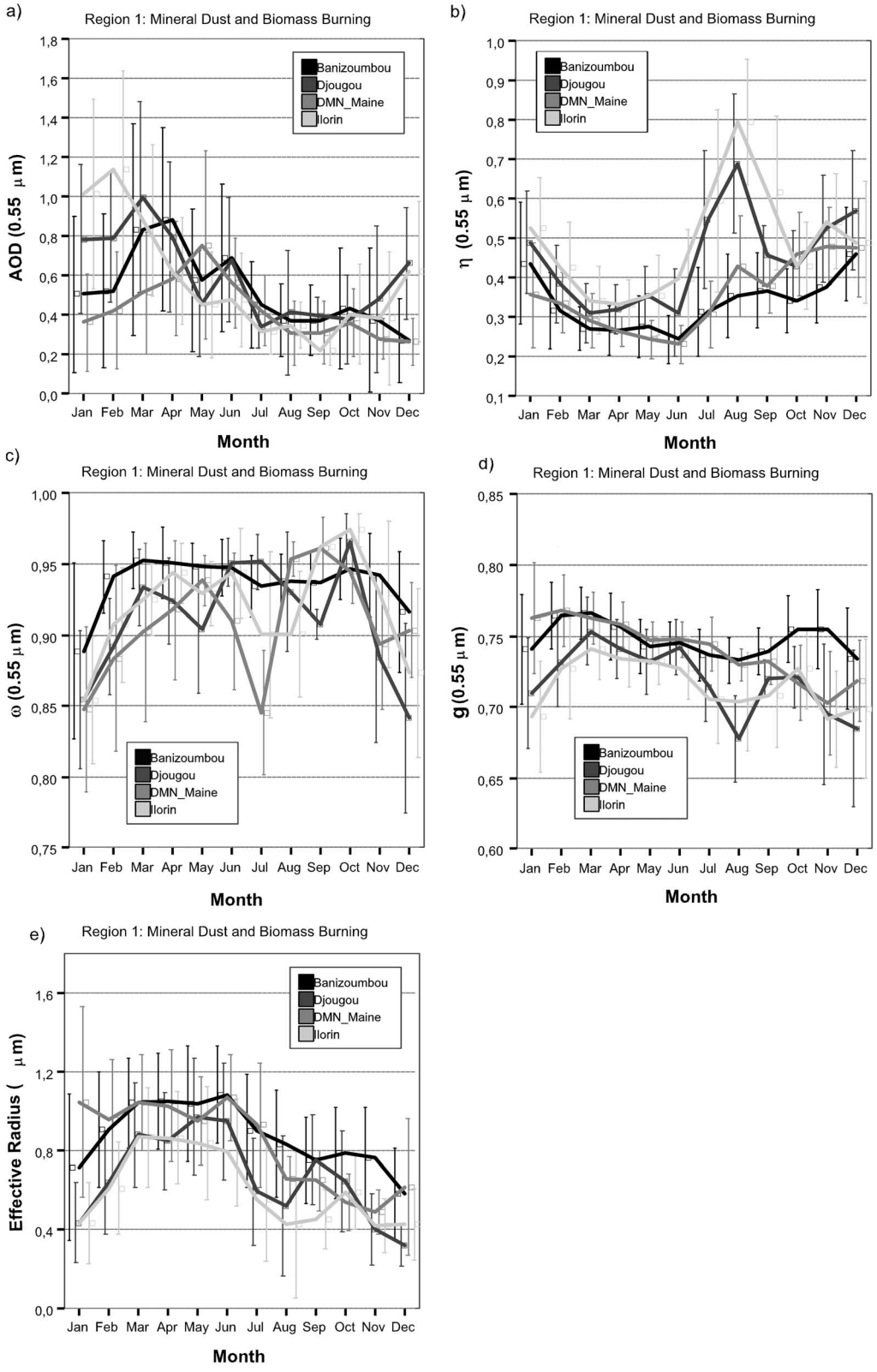

Figure 2. Interannual monthly average of (a) aerosol optical depth (AOD), (b) fine aerosol fraction η, (c) single scattering albedo ω, (d) asymmetry factor g, all at 0.55 μm, and (e) effective radius for region 1. Error bars indicate standard deviations.

Table 1. Interannual Average of Aerosol Properties Derived by AERONET for Each Region by Season[a]

Season,[b] Aerosol[c]	Central Africa, Region 1		Asia, Region 2	
	DJF, BB+MD	MAM, MD	MAM, UI+MD	JJA, UI
N_ω/N_E (%)	66/88	65/96	42/84	51/83
AOD (0.55 μm)	0.6 ± 0.4	0.8 ± 0.5	0.3 ± 0.3	0.4 ± 0.2
ω(0.44/0.55/0.67/0.87/1.02)	0.86/0.88/0.90/0.91/0.92 ± (0.05–0.06)	0.91/0.93/0.95/0.96/0.96 ± (0.03–0.04)	0.92/0.93/0.94/0.93/0.93 ± (0.02–0.05)	0.95/0.95/0.94/0.93/0.93 ± (0.03–0.04)
m(0.44/0.55/0.67/0.87/1.02)	1.41/1.43/1.45/1.44/1.43 ± (0.05–0.06)	1.47/1.48/1.49/1.47/1.46 ± (0.04–0.05)	1.46/1.47/1.49/1.50/1.49 ± (0.04–0.06)	1.41/1.42/1.42/1.42/1.42 ± (0.04–0.06)
k(0.44/0.55/0.67/0.87/1.02)	0.011/0.009/0.008/0.007/0.006 ± (0.006–0.009)	0.004/0.003/0.002/0.002/0.002 ± (0.002–0.003)	0.007/0.006/0.005/0.006/0.006 ± (0.003–0.004)	0.007/0.007/0.007/0.007/0.008 ± (0.004–0.008)
g(0.44/0.55/0.67/0.87/1.02)	0.75/0.73/0.72/0.72/0.73 ± (0.04–0.05)	0.77/0.76/0.74/0.74/0.75 ± 0.02	0.71/0.68/0.66/0.65/0.65 ± (0.02–0.04)	0.73/0.70/0.67/.63/0.61 ± (0.03–0.04)
η (0.55 μm)	0.4 ± 0.1	0.3 ± 0.1	0.6 ± 0.2	0.9 ± 0.1
r_{eff} (μm)	0.6 ± 0.3	1.0 ± 0.3	0.4 ± 0.2	0.3 ± 0.1
Esf. (%)	6 ± 1	2 ± 1	24 ± 2	74 ± 1

[a]The error assigned to each average value is the standard deviation except for the sphericity parameter (Esf.), where mean typical error is shown. N_ω is the percentage of available data for calculating ω, m, and k, while with N_E is obtained Esf. N_E and Nω are calculated using total data by season.
[b]Season DJF is Dec.–Feb., MAM is Mar.–May, and JJA is Jun.–Aug.
[c]Aerosol type BB is biomass burning, MD is mineral dust, and UI is urban-industrial.

(0.3 ± 0.3) and effective radius associated with a notable decrease in the parameter η. The observed η values during this period, 0.6–0.8, are higher than those recorded under the influence of pure mineral dust for region 1 in the spring (~0.3–0.4), which could indicate a combined contribution of dust and urban-industrial aerosols. Aerosol levels diminish after July and August, coinciding with the beginning of the Asian monsoon rainy season and reaching minimal values during autumn and early winter. During this gradual AOD decrease it is possible to distinguish two different periods with respect to the fine fraction values, which indicates a slight change in anthropogenic contributions. Thus, the η average value in summer, from June to August, is 0.9 ± 0.1, a typical value of anthropogenic aerosols [*Kaufman et al.*, 2005; *García*, 2009] compared to 0.7 ± 0.2 during the autumn and winter. During these seasons (September–November (SON) and DJF) there was also an increase of aerosol-absorbing properties with respect to those recorded in summer. For example, during the autumn the interannual average of ω(0.44/0.67/0.87/1.02 μm) was 0.94/0.92/0.91/0.91 ± (0.02–0.03) for Anmyon station; values lower than the ones observed at this station during the summer, 0.95/0.95/0.95/0.94 ± (0.02–0.03) (Figure 3c). Similar behaviour was observed for other radiative properties, such as the imaginary part of refractive index (data not shown). The effective radius also clearly changes, and reaches minimum values in the summer followed by an increase in autumn and winter (Figure 3e).

[20] The mixture of urban-industrial and mineral dust particles is evident in the regional averages of the aerosol properties of size and shape for spring, which is the representative period of the mixed aerosols, as shown in Table 1. The contribution of mineral dust modifies the properties associated with dispersive processes, increasing the effective radius of the particle distribution, the nonsphericity, and the real part of the refractive index, which modify the scattering patterns. In addition, the contribution of these larger particles increments the scattering optical depth at longer wavelengths (0.87 and 1.02 μm) and increases the ω values at these wavelengths with regard to the shorter ones (see Table 1) [*Eck et al.*, 2003; *Dubovik et al.*, 2006]. Thus, the mixture with mineral dust during spring results in a modulation of the spectral radiative properties. Conversely, the summer average values of the radiative properties are very similar to those in European urban-industrial environments [*Dubovik et al.*, 2002; *García*, 2009].

4. Discussion

[21] Surface albedo (SA) is the second parameter (besides aerosol properties) that determines aerosol effect on climate. This fact modulates aerosol radiative forcing, even changing its sign [e.g., *Sokolik and Toon*, 1997; *Balkanski et al.*, 2007]. Atmospheric aerosols have a high spatial and temporal variability, and are frequently transported in trans-oceanic conditions, extending over regions with different surface albedo. Oceanic and vegetation zones are less bright, with SA generally less than 0.18 while the desert regions are brighter areas with SA between 0.18 and 0.50. Note that the regions covered by ice or snow are the brightest areas of the planet (SA > 0.50), however they are not considered in the current study. These values are obtained from the average

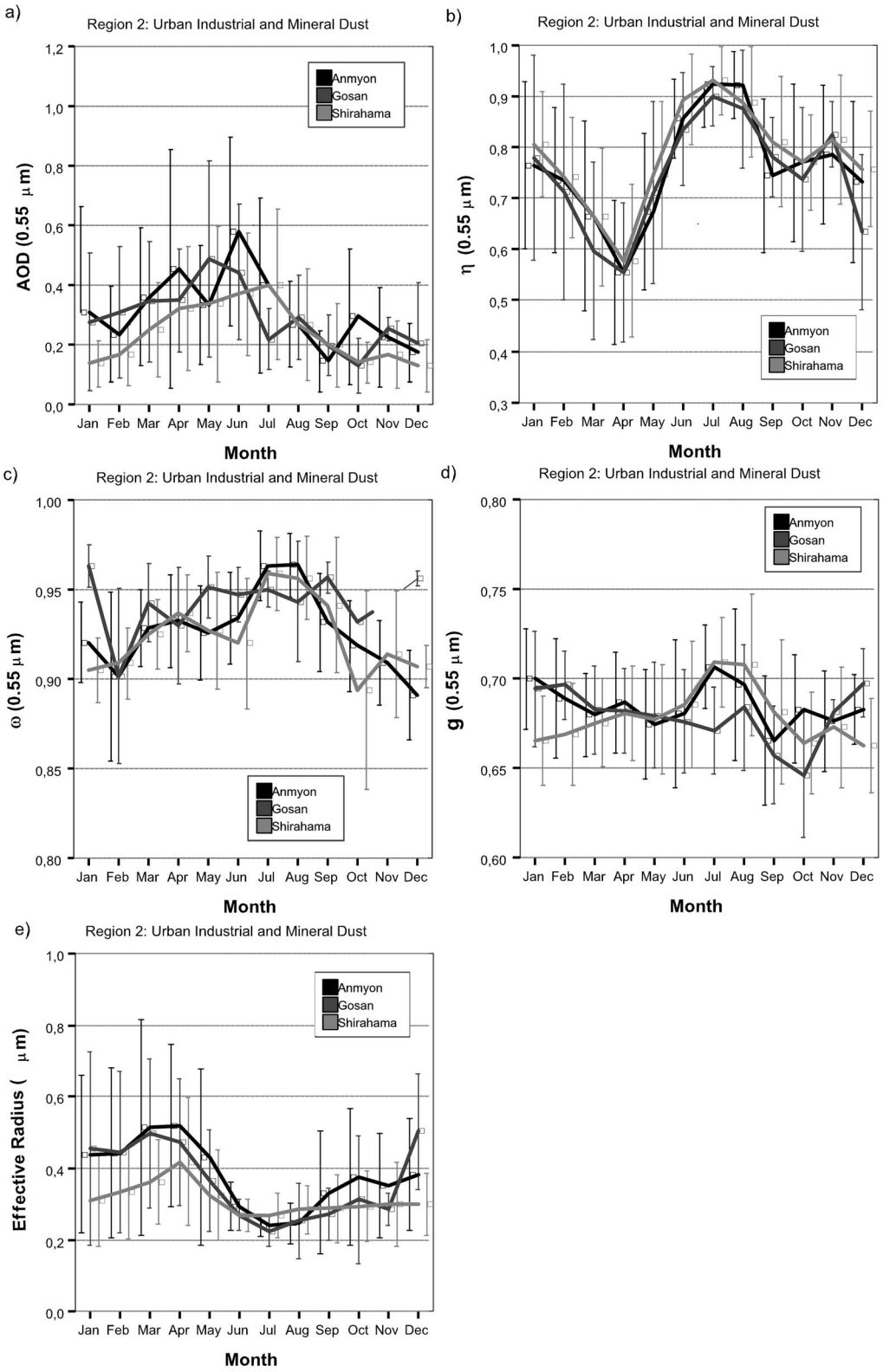

Figure 3. Interannual monthly average of (a) aerosol optical depth (AOD), (b) fine aerosol fraction η, (c) single scattering albedo ω, (d) asymmetry factor g, all at 0.55 μm, and (e) effective radius for region 2. Error bars indicate standard deviations.

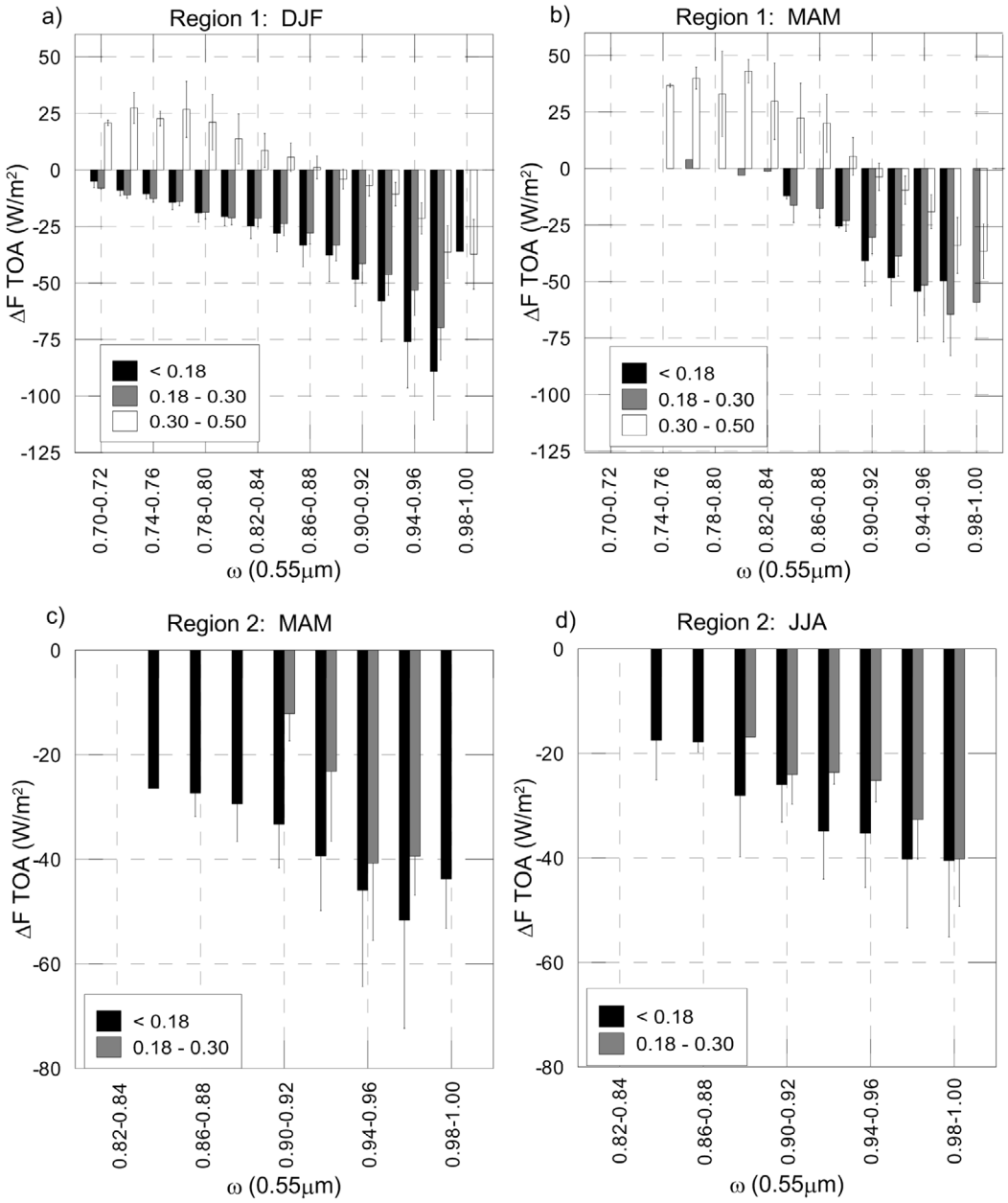

Figure 4. Aerosol radiative forcing average, ΔF (W m^{-2}), at the TOA versus single scattering albedo at 0.55 μm, ω, by intervals of surface albedo of <0.18, 0.18–0.30, and 0.30–0.50 for region 1 for (a) winter (DJF) and (b) spring (MAM); and for region 2 for (c) spring (MAM) and (d) summer (JJA). Error bars indicate standard deviations.

of spectral surface albedo derived by AERONET V2.0 at 0.44, 0.67, 0.87, and 1.02 μm for the stations considered in this study, as reported in the works by *Zhou et al.* [2005] and *Balkanski et al.* [2007].

[22] The data were grouped by surface reflectance values and by seasons in both regions in order to analyze the influence of surface albedo, as shown in Figure 4. This plot represents radiative forcing versus single scattering albedo for different intervals of surface albedo. Note that only those cases with AOD(0.44 μm) $\geq$ 0.4, at which the AERONET ω values are derived, were considered. Figures 5a and 5b show the number of occurrences of single scattering albedo for each interval and for the three SA ranges.

4.1. Region 1: Mineral Dust and Biomass Burning

[23] In region 1 (Figures 4a and 4b), with increasing absorption capacity of aerosol (low ω), solar irradiance levels decrease both at the BOA and TOA, causing an increase of the radiative forcing at the surface and a decrease (in absolute value) in the upper atmosphere. Radiative forcing values shown at the TOA for the darkest surfaces, SA < 0.18, indicate that the mineral dust cools the atmospheric column for any single scattering albedo value. For intermediate situations, 0.18–0.30, radiative forcing of mineral dust is similar to those obtained with oceanic reflectivities (<0.18). For the brightest areas such as deserts, 0.30–0.50, the sign of

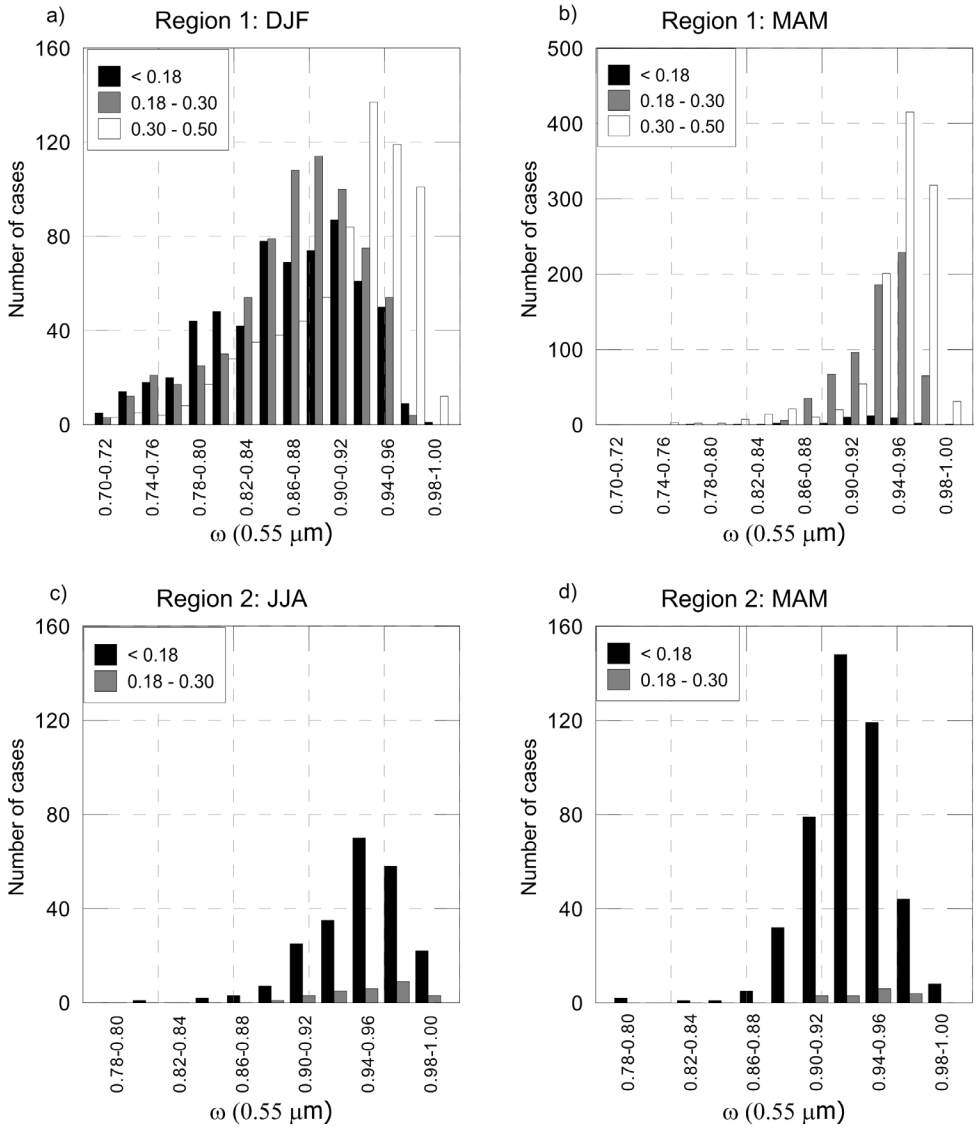

Figure 5. Number of cases of radiative forcing at the TOA versus single scattering albedo at 0.55 μm, ω, by intervals of surface albedo of <0.18, 0.18–0.30, and 0.30–0.50 for region 1 for (a) winter (DJF) and (b) summer (JJA); and for region 2 for (c) spring (MAM) and (d) summer (JJA).

radiative forcing in the upper atmosphere basically depends on two factors, size distribution and mineralogical composition of the aerosol, which determine the single scattering albedo. For ω(0.55 μm) greater than ~0.88 the net effect of mineral dust is a cooling of the atmosphere, while below this threshold there is a clear change in the trend, resulting in a warming effect. Under these conditions, ω(0.55 μm) < 0.88, the warming, on average, is 10 ± 11 Wm^{-2} for the mixture of mineral dust and biomass burning (during DJF), while a value of 28 ± 16 Wm^{-2} is found under the presence of pure mineral dust (during MAM). These results enhance the warming effect of the greenhouse gases. Although these situations occur both during DJF (Figure 4a) and MAM (Figure 4b), they are predominant in DJF, and account for 66% of cases reported with ω(0.55 μm) < 0.88 for SA between 0.30 and 0.50, compared with 21% during MAM. Therefore, on desert surfaces it is important to pay particular attention to those mixture conditions that increase aerosol absorption capacity.

[24] In Figure 4 also note that for nonabsorbing aerosols (ω(0.55 μm) > 0.88) forcing values increase as the surface is less reflective, whereas for absorbing aerosols just the opposite occurs (in absolute values). This behavior is due to the differences in the reflectivity of the aerosol layer compared with the surface. For nonabsorbing aerosols the differences in the backscattering solar radiation, under clean conditions with respect to aerosol situations, is reduced when surface albedo increases. However, for absorbing aerosols the backscattering solar radiation is lesser than nonabsorbing aerosols, and consequently surfaces with higher reflectivity have greater backscattering solar radiation in clean conditions (positive radiative forcing). There are also a larger number of multiple reflections between the surface and the aerosol layer; therefore, the multiple scattering

Table 2. Interannual Average of Aerosol Radiative Forcing, ΔF (Wm^{-2}), at the BOA and the TOA and Aerosol Optical Depth, AOD, at 0.55 μm for Regions 1 and 2 by Season and by Range of Surface Albedo (SA)

	Season, Aerosol	SA	ΔF_{BOA}	ΔF_{TOA}	AOD (0.55 μm)
Central Africa Region 1	DJF, BB+MD	0–0.30	−130 ± 44	−34 ± 18	0.8 ± 0.4
		0.30–0.50	−66 ± 35	−4 ± 14	0.4 ± 0.3
	MAM, MD	0–0.30	−102 ± 42	−38 ± 18	0.8 ± 0.4
		0.30–0.50	−88 ± 41	−15 ± 18	0.7 ± 0.5
Asia Region 2	MAM, UI+MD	0–0.30	−58 ± 31	−27 ± 15	0.3 ± 0.3
	JJA, UI	0–0.30	−49 ± 26	−24 ± 14	0.4 ± 0.2

processes and absorption rise. These effects are more evident in the upper atmosphere than in the surface, although they occur in both cases. Note that for each ω interval (Figure 4) the error bars represent the uncertainties in ΔF due to variations in AOD and in other factors, such as aerosol microphysical properties.

[25] In order to compare the radiative effect of mineral dust interannual averages of ΔF were assessed in each region by season (Table 2). No significant differences between the corresponding ΔF values or trends were found at both the TOA and BOA for the intervals of surface albedo SA < 0.18 and SA < 0.30, as is also shown in Figure 4 at the TOA. Thus, interannual averages of ΔF at the TOA and the BOA have been evaluated by differentiating only two ranges of SA, 0–0.30 and 0.30–0.50, during the different seasons.

[26] Note that the decrease in ΔF absolute values at the TOA (Figure 4a) is primarily due to the absorption of the biomass burning particles. This process reduces the amount of energy backscattered towards the top of the atmosphere, keeping more solar energy in it. Along with this, we must also take into account two other factors: The higher reflectance of a layer of mineral dust with regard to a mixed situation, contributing to higher ΔF at the TOA [*Derimian et al.*, 2008] and the difference in the scattering patterns associated with the size of the particles in each season: r_{eff} = 0.6 ± 0.3 μm for DJF and r_{eff} = 1.0 ± 0.3 μm for MAM. At the BOA, the AOD is the primary factor that determines the ΔF values (maximum ΔF values are associated with the highest AOD levels, Table 2) although it is necessary to know the absorption properties and scattering pattern of the particles to obtain a complete description of the ΔF values.

[27] These results are consistent with those found elsewhere for similar mixture situations (mineral dust and biomass burning). For example, *Li et al.* [2004] found that pure mineral dust was ~35% more efficient than the mixture at the TOA and ~25% lower at the BOA for the oceanic region of the African coast, 15°–25°N and 45°–15°W, where SA < 0.30. In addition, *Derimian et al.* [2008] found that, for conditions with low reflectivity (M'Bour station in Senegal during the African Monsoon Multidisciplinary Analyses campaign), the desert dust at the TOA was between 82% and 200% more efficient than when it was mixed with biomass burning particles, while at the surface this mixture increased the efficiency of mineral dust by between 10% and 90%.

4.2. Region 2: Urban-Industrial and Mineral Dust

[28] In region 2 the radiative influence of mixing mineral dust with urban-industrial aerosols was analyzed considering spring, as was discussed in section 3.2, while the summer was taken as representative of pure urban-industrial aerosols. During these seasons there were no cases with surface albedo higher than 0.30 and, unlike the results in region 1, the effect of surface albedo is not as important in radiative forcing, as Figures 4c and 4d show for spring and summer, respectively. Note that there is no change in the sign of the radiative forcing. Figures 5c and 5d show the number of occurrences of single scattering albedo for each interval and for the three SA ranges. Although with increasing surface albedo the ΔF values decrease (in absolute value), both at the TOA and BOA, the trend among intervals of surface albedo (<0.18 and 0.18–0.30) is the same. Therefore, to analyze the ΔF the stations were grouped without considering surface albedo intervals (Table 2).

[29] Even though the average values of AOD are similar in both periods (0.3 ± 0.3 in MAM and 0.4 ± 0.2 in JJA), ΔF at the BOA and TOA is higher (in absolute terms) when mineral dust is mixed with urban-industrial aerosols, that is, −58 ± 31 and −27 ± 15 Wm^{-2} at the BOA and TOA, respectively, during spring, and −49 ± 26 Wm^{-2} at the BOA and −24 ± 14 Wm^{-2} at the TOA during summer. These differences are mainly attributed to the difference in the scattering processes associated with the increase of particle size, along with a lower sphericity during the mixing time, since the absorbent capacity of the aerosol (ω and k) is, on average, similar (see Table 1).

[30] These results are consistent with those cited in the literature. For example, *Conant et al.* [2003], among other authors, found that mineral dust at the TOA is 8% more efficient than the urban-industrial, in pure conditions, and 9% more efficient at the BOA for the East Asia region (Asian Pacific Regional Aerosol Characterization Experiment campaign in 2001). *Gu et al.* [2006] studied the climatic effects of different aerosol types in China simulated by the UCLA general circulation model. They analyzed five different aerosol situations, where their DUST model is based on 90% large mineral dust particles (8.0 μm) and 10% soot, whereas their SOOT model uses 100% soot, and found radiative forcing values at TOA of 30.97 Wm^{-2} and 21.71 Wm^{-2} for SOOT and DUST models, respectively. Although those values are similar to those shown in Table 2, notice that the experimental setup of those simulations does not reproduce the conditions at the stations used in the present work (distinct single scattering albedo and effective radius).

5. Conclusions

[31] Radiative properties of mixed aerosols were assessed and analyzed in two regions. In region 1 (Central Africa)

mineral dust is the dominant aerosol and the effect of biomass burning is an increase the absorption properties of the mineral dust. We found that when mineral dust is mixed with biomass burning it is essential to take into account the surface albedo when evaluating the radiative forcing. This parameter could even modify the sign of this magnitude at the TOA, that is, it is possible to change from a situation of negative forcing (cooling the system) to a positive one (warming). This occurs for ω values at 0.55 μm of less than 0.88 with highly reflective surfaces (SA between 0.30 and 0.50). For low SA (<0.30) we found that the effect of aerosols is always to cool the Earth-atmosphere system. Under pure dust conditions the change in the sign of forcing is observed in the ω interval 0.88–0.90 for the higher SA interval. On the other hand, in region 2 (Asia) the contribution of mineral dust mainly modifies those properties associated with scattering processes (the average particle size and sphericity parameter). Moreover, it is also observed that forcing values of the mixture at TOA are higher than those recorded in pure conditions for the same range of single scattering albedo.

[32] On average, we obtained the highest ΔF values for the mixture of mineral dust and biomass burning aerosols: -130 ± 44 Wm^{-2}. This value corresponds to Central Africa at the BOA and for surfaces with low reflectance (SA < 0.18), whereas when only mineral dust is considered the ΔF is -102 ± 42 Wm^{-2}. For the Asian region and under the same conditions, the ΔF values are half of the above; again higher ΔF values are obtained for the aerosol mixture. Nevertheless, the ΔF calculated at the TOA gives similar results for both the mixture situation and for the dominant aerosol: -34 ± 18 and -38 ± 18 Wm^{-2}, respectively, for region 1 and -27 ± 15 and -24 ± 14 Wm^{-2}, respectively, for region 2.

[33] **Acknowledgments.** Support for this study was given by Spanish Ministry of Education and Science, projects CGL2005-03428-C04-02, CGL2007-66477-C02-02/CLI, PI042005/033, and CGL2008-04740/CLI. We gratefully acknowledge the data provided by AERONET network and wish to express our appreciation to the station operators for their help in running the instruments.

References

Arimoto, R., et al. (2006), Characterization of Asian Dust during ACE-Asia, *Global Planet. Change*, *52*, 23–56.

Balkanski, Y., M. Schulz, T. Claquin, and S. Guibert (2007), Reevaluation of mineral aerosol radiative forcing suggests a better agreement with satellite and AERONET data, *Atmos. Chem. Phys. Disc.*, *7*, 81–95.

Chung, S. H., and J. H. Seinfeld (2005), Climate response of direct radiative forcing of anthropogenic black carbon, *J. Geophys. Res.*, *110*, D11102, doi:10.1029/2004JD005441.

Conant, W. C., J. H. Seinfeld, J. Wang, G. R. Carmichael, Y. Tang, I. Uno, P. J. Flatau, K. M. Markowicz, and P. K. Quinn (2003), A model for the radiative forcing during ACE-Asia derived from CIRPAS Twin Otter and *R/V Ronald H. Brown* data and comparison with observations, *J. Geophys. Res.*, *108*(D23), 8661, doi:10.1029/2002JD003260.

Cox, C., and W. Munk (1954), The measurements of the roughness of the sea surface from photographs of the Sun's glitter, *J. Opt. Soc. Am.*, *44*, 838–850.

D'Almeida, J. A., P. Koepke, and E. P. Shettle (1991), *Atmospheric Aerosols. Global Climatology and Radiative Characteristics*, 561 pp., A. Deepak, Hampton, Va.

Derimian, Y., J.-F. Léon, O. Dubovik, I. Chiapello, D. Tanré, A. Sinyuk, F. Auriol, T. Podvin, G. Brogniez, and B. N. Holben (2008), Radiative properties of aerosol mixture observed during the dry season 2006 over M'Bour, Senegal (African Monsoon Multidisciplinary Analysis campaign), *J. Geophys. Res.*, *113*, D00C09, doi:10.1029/2008JD009904.

Dubovik, O., and M. King (2000), A flexible inversion algorithm for retrieval of aerosol optical properties from Sun and sky radiance measurements, *J. Geophys. Res.*, *105*, 20,673–20,696, doi:10.1029/2000JD900282.

Dubovik, O., B. N. Holben, T. F. Eck, A. Smirnov, Y. J. Kaufman, M. D. King, D. Tanré, and I. Slutsker (2002), Variability of absorption and optical properties of key aerosol types observed in worldwide locations, *J. Atmos. Sci.*, *59*, 590–608.

Dubovik, O., et al. (2006), Application of light scattering by spheroids for accounting for particle nonsphericity in remote sensing of desert dust, *J. Geophys. Res.*, *111*, D11208, doi:10.1029/2005JD006619.

Dubuisson, P., J. C. Buriez, and Y. Fouquart (1996), High spectral resolution solar radiative transfer in absorbing and scattering media, application to the satellite simulation, *J. Quant. Spectrosc. Radiat. Transfer*, *55*, 103–126.

Dubuisson, P., D. Dessailly, M. Vesperini, and R. Frouin (2004), Water vapor retrieval over ocean using near-infrared imagery, *J. Geophys. Res.*, *109*, D19106, doi:10.1029/2004JD004516.

Eck, T. F., et al. (2003), Variability of biomass burning aerosol optical characteristics in southern Africa during the SAFARI 2000 dry season campaign and a comparison of single scattering albedo estimates from radiometric measurements, *J. Geophys. Res.*, *108*(D13), 8477, doi:10.1029/2002JD002321.

García, O. E., et al. (2008a), Validation of AERONET estimates of atmospheric solar fluxes and aerosol radiative forcing by ground-based broadband measurements, *J. Geophys. Res.*, *113*, D21207, doi:10.1029/2008JD010211.

García, O. E., A. M. Díaz, F. J. Expósito, J. P. Díaz, A. Redondas, and T. Sasaki (2008b), Aerosol radiative forcing and forcing efficiency in the UVB for regions affected by Saharan and Asian mineral dust, *J. Atmos. Sci.*, *66*, 1033–1040, doi:10.1175/2008JAS2816.1.

García, O. E. (2009), Estudio de las propiedades radiativas de los aerosoles atmosféricos mediante técnicas de teledetección, Doctoral Thesis, University of La Laguna, Spain.

Gu, Y., K. N. Liou, Y. Xue, C. R. Mechoso, W. Li, and Y. Luo (2006), Climatic effects of different aerosol types in China simulated by the UCLA general circulation model, *J. Geophys. Res.*, *111*, D15201, doi:10.1029/2005JD006312.

Hall, D. K., G. A. Riggs, and V. V. Salomonson (2002), MODIS/Terra Snow Cover Daily L3 Global 0.05Deg CMG V004, February 2000 to Present, http://nsidc.org, Natl. Snow and Ice Data Cent., Boulder, Colo. (updated daily)

Hansen, J., and L. Nazarenko (2004), Soot climate forcing via snow and ice albedos, *Proc. Natl. Acad. Sci. U.S.A.*, *101*, 423–428.

Holben, B. N., et al. (2001), An emerging ground-based aerosol climatology: Aerosol optical depth from AERONET, *J. Geophys. Res.*, *106*, 12,067–12,097.

Intergovernmental Panel on Climate Change (IPCC) (2007), *Climate Change 2007: Synthesis Report*, Geneva, Switzerland.

Kaufman, Y. J., I. Koresn, L. A. Remer, D. Tanré, P. Ginoux, and S. Fan (2005), Dust transport and deposition observed from the Terra-Moderate Resolution Imaging Spectroradiometer (MODIS) spacecraft over the Atlantic Ocean, *J. Geophys. Res.*, *110*, D10S12, doi:10.1029/2003JD004436.

Lacis, A. A., and V. Oinas (1991), A description of the correlated *k* distribution method for modeling nongray gaseous absorption, thermal emission, and multiple scattering in vertically inhomogeneous atmosphere, *J. Geophys. Res.*, *96*, 9027–9063 doi:10.1029/90JD01945.

Li, F., A. M. Vogelmann, and V. Ramanathan (2004), Saharan dust aerosol radiative forcing measured from space, *J. Clim.*, *17*, 2558–2571.

Lucht, W., and J. L. Roujean (2000), Consideration in parametric modeling of BRDF and albedo from multiangular satellite sensors observations, *Remote Sens. Rev.*, *18*, 343–379.

Lyamani, H., F. J. Olmo, A. Alcántara, and L. Alados-Arboledas (2006), Atmospheric aerosols during the 2003 heat wave in southeastern Spain II: Microphysical columnar properties and radiative forcing, *Atmos. Environ.*, *40*, 6465–6476.

Martins, J. V., P. Artaxo, C. Liousse, J. S. Reid, P. V. Hobbs, and Y. J. Kaufman (1998), Effects of black carbon content, particle size, and mixing on light absorption by aerosols from biomass burning in Brazil, *J. Geophys. Res.*, *103*, 32,041–32,050, doi:10.1029/98JD02593.

Moody, E. G., M. D. King, S. Platnik, C. B. Schaaf, and F. Gao (2005), Spatially complete global spectral surface albedos: Value-added datasets derived from terra MODIS land products, *IEEE Trans. Geosci. Remote Sens.*, *43*, 144–158.

Nakajima, T., and M. Tanaka (1988), Algorithms for radiative intensity calculations in moderately thick atmospheres using a truncation approximation, *J. Quant. Spectrosc. Radiat. Transfer*, *40*, 51–69.

Nolin, A., R. L. Armstrong, and J. Maslanik (1998), Near Real-Time SSM/I EASE-Grid Daily Global Ice Concentration and Snow Extent, January 1998 to Present, http://nsidc.org, Natl. Snow and Ice Data Cent., Boulder, Colo. (updated daily).

Prospero, J. M., P. Ginoux, O. Torres, S. E. Nicholson, and T. E. Gill (2002), Environmental characterization of global sources of atmospheric soil dust identified with the NIMBUS 7 Total Ozone Mapping Spectrometer (TOMS) absorbing aerosol product, *Rev. Geophys.*, *40*(1), 1002, doi:10.1029/2000RG000095.

Roger, J. C., M. Mallet, P. Dubuisson, H. Cachier, E. Vermote, O. Dubovik, and S. Despiau (2006), A synergetic approach for estimating the local direct aerosol forcing: Application to an urban zone during the ESCOMPTE experiment, *J. Geophys. Res.*, *111*, D13208, doi:10.1029/2005JD006361.

Satheesh, S. K., and K. K. Moorthy (2005), Radiative effects of natural aerosols: A review, *Atmos. Environ.*, *39*, 2089–2110.

Smirnov, A., B. N. Holben, A. Lyapustin, I. Slutsker, and T. F. Eck (2004), AERONET processing algorithms refinement, AERONET Workshop, May 10–14 2004, El Arenosillo, Spain.

Sokolik, I. N., and O. B. Toon (1997), Direct radiative forcing by anthropogenic airborne mineral aerosols, *Nature*, *381*, 681–685, doi:10.1038/381681a0.

Stamnes, K., S. C. Tsay, W. Wiscombe, and K. Jayaweera (1988), Numerically stable algorithm for discrete-ordinate-method radiative transfer in multiple scattering and emiting layered media, *Appl. Opt.*, *27*, 2502–2509.

Zhou, M., H. Yu, R. E. Dickinson, O. Dubovik, and B. N. Holben (2005), A normalized description of the direct effect of key aerosol types on solar radiation as estimated from aerosol robotic network aerosols and moderate resolution imaging spectroradiometer albedos, *J. Geophys. Res.*, *110*, D19202, doi:10.1029/2005JD005909.

A. M. Díaz, J. P. Díaz, and F. J. Expósito, Grupo de Observación de la Tierra y la Atmósfera, Universidad de La Laguna, A/Astrofisico Fco. Sanchez s/n, La Laguna, E-38200 Tenerife, Spain.

O. E. García, Centro de Investigación de Izaña, Agencia Estatal de Meteorología, C/La Marina, 20 (6º planta), Santa Cruz de Tenerife, E-38001 Tenerife, Spain. (ogarciar@aemet.es)